Spectral method for a kinetic swarming model

I. Gamba, J. Haack, S. Motsch

May 17, 2015

Abstract

In this paper we present the first numerical method for a kinetic description of the Vicsek swarming model. The kinetic model poses a unique challenge, as there is a distribution dependent collision invariant to satisfy when computing the interaction term. We use a spectral representation linked with a discrete constrained optimization to compute these interactions. To test the numerical scheme we investigate the kinetic model at different scales and compare the solution with the *microscopic* and *macroscopic* descriptions of the Vicsek model. We observe that the kinetic model captures key features such as vortex formation and traveling waves.

Contents

1 Introduction

Swarming behavior is a perfect illustration of multiscale phenomena. In a flock of birds for instance one can either decide to model each individual separately [2,3,14,35,36], or one can model the whole flock as a single entity [13,29,38,39]. These two points-of-view have led to two different types of models for swarming: *microscopic* models (a.k.a agent-based-models) and *macroscopic* models involving macroscopic quantities (e.g. mass, flux). In this work, we use an intermediate approach studying a swarming model at the *kinetic* scale (also called the mesoscopic scale).

Kinetic models offer the same possibilities as microscopic models to model phenomena. For instance, one can model complex interactions among agents or introduce various boundary conditions in a kinetic model. Macroscopic models are less flexible from this point of view. Meanwhile, kinetic models allow for analytic study, which is more scarce in microscopic models. Rigorous derivation of kinetic models from a microscopic model can be achieved in some cases, however, one needs to have the number of particles to tend to infinity. In gas dynamics, this would mean that the mean free path between particle interactions becomes small enough. Unfortunately, there is no convenient mean free path concept in swarming models. For this reason, it is also crucial to numerically connect kinetic models with their corresponding microscopic models.

Several works have already studied kinetic models for swarming [12,15,26], but few have done a numerical investigation. In this work, we first introduce a numerical scheme for a kinetic swarming model based on the Vicsek model. We then investigate numerically the model at different scales using the corresponding *microscopic*, *kinetic*, and *macroscopic* models. In particular, we emphasize how the kinetic model is able to capture typical solutions of both microscopic and macroscopic models.

Numerical solution of kinetic equations has long been a computational challenge due to the typically integro-differential nature of the interactions between particles, as well as the higher dimensionality of phase space. In particular, the kinetic model that has been most studied is the Boltzmann transport equation of rarefied gas dynamics. Stochastic methods, most notably Direct Simulation Monte Carlo [4], have long been the primary method of solution for these problems due to the reduction of dimensionality. However, these methods suffer from the presence of noise in their solutions owing to the stochastic nature of their solution, and can become very expensive in problems that are far from equilibrium or problems with transients.

Since the creation of the DSMC method, the considerable increase of computational power has made deterministic computation of kinetic equations within the realm of possibility, despite the expense of dimensionality. Discrete velocity methods [10, 11, 30] simulate particle interactions on a mesh in velocity space, but can suffer from low accuracy and lack of conservation [11, 25, 27, 37]. Spectral methods exploit the weighted convolution structure of the Fourier transform [5] of the interaction terms for high accuracy. Spectral approximations for Boltzmann collision operators were first proposed by Pareschi and Perthame [32], and many other authors developed numerical methods for Boltzmann and Fokker-Planck type collisions [6, 7, 18, 20–23, 33, 34].

In this paper we present a novel spectral method for computing the kinetic form of the Vicsek model, in fact the first numerical method for this kinetic formulation. This model presents several new challenges for a numerical method. The alignment interaction between particles gives a nonlinear integro-differential operator that needs to be handled carefully. By reformulation in terms of the mean direction of motion of the particles, we obtain a nonlinear diffusion-like operator. We then take the Fourier transform and use orthogonality to obtain a coupled set of equations.

This nonlinear interaction gives rise to collision invariants, in the spirit of the Boltzmann collision operator, which are needed to obtain a hydrodynamic limit for the model. These invariant properties must also be preserved at the discrete level, and we perform a constrained optimization in a suitable norm of the solution obtained by the spectral method to ensure that the invariants are correctly preserved. We show that this preservation is crucial by comparing the solution with and without preservation of the collision invariants.

Numerical tests are performed comparing the solution of the kinetic equation to both the macroscopic and microscopic models. We first investigate the kinetic model in a 'hydrodynamic limit' by performing a change of scales. We observe the emergence of traveling waves (e.g. rarefaction and shock waves) that match perfectly with the solutions of the macroscopic model. Those numerical results are remarkable as there is no analytic theory to handle traveling waves for the macroscopic model (the model being non-conservative). We then compare the kinetic model with the 'microscopic model'. For that, we take advantage that boundary conditions are easily implemented at the microscopic and kinetic level. We perform simulations in a closed domain with reflexive boundary conditions. We observe the emergence of vortex formation for the two models and compare the solutions.

The paper is organized as follows: in Section 2, we introduce the swarming model referred to as the Vicsek model at different scales (microscopic, kinetic, and macroscopic). In Section 3, we develop a numerical scheme (spectral method) for the kinetic model that preserves the so-called generalized collisional invariant. Numerical investigations comparing the model at different scales are presented in Section 4. We close with a discussion of future work in this area.

2 Self-organized dynamics at different scales

In this section, we introduce the model of self-organized dynamics at different scales. Based on the Vicsek model [16, 40], we first introduce a particle system describing alignment behavior. Next, we give a short review on the kinetic equation associated with these dynamics and discuss the collisional invariants, whose properties play a central role in the development of the numerical scheme [31]. Finally, we introduce the macroscopic limit of the dynamics.

2.1 Microscopic model

At the *microscopic* level, the Vicsek model describes the evolution of N particles which tend to align with their neighbors. Each particle is represented by a position, $\mathbf{x}_k \in \mathbb{R}^d$, and a unit velocity vector, $\omega_k \in \mathbb{S}^{d-1}$. The evolution of the particles is governed by the following dynamical system:

$$\frac{d\mathbf{x}_k}{dt} = \omega_k \quad , \quad d\omega_k = P_{\omega^\perp}\Big(\Omega_k dt + \sqrt{2\sigma}\, dB_t^k\Big). \tag{2.1}$$

Here, Ω_k denotes the mean velocity:

$$\Omega_k = \frac{\sum_{|\mathbf{x}_j - \mathbf{x}_k| < R} \omega_j}{\left|\sum_{|\mathbf{x}_j - \mathbf{x}_k| < R} \omega_j\right|}, \tag{2.2}$$

with R the radius of interaction, $\sigma > 0$ is the intensity of the noise with B_t^k the Brownian motion. The matrix $P_{\omega^\perp}$ is a projector:

$$P_{\omega^\perp} = \mathrm{Id} - \omega \otimes \omega, \tag{2.3}$$

which enforces the velocity ω_k to remain of norm 1.

2.2 Kinetic model

Following the characteristics of the system (2.1), one can write the evolution of the density of particles $f^N(t, \mathbf{x}, \omega)$. Formally, in the limit $N \to \infty$, the density of particles f satisfies the following kinetic equation:

$$\partial_t f + \omega \cdot \nabla_{\mathbf{x}} f + \nabla_\omega \cdot (F[f] f) = \sigma \Delta_\omega f, \tag{2.4}$$

with the vector fields $F[f](\mathbf{x},\omega)$ given by:

$$F[f](\mathbf{x},\omega) = (\mathrm{Id} - \omega \otimes \omega)\Omega(\mathbf{x}) \quad , \quad \Omega(\mathbf{x}) = \frac{J(\mathbf{x})}{|J(\mathbf{x})|}. \tag{2.5}$$

Here, $J(\mathbf{x})$ denotes the mean flux at position $\mathbf{x}$:

$$J(\mathbf{x}) = \int_{\mathbf{y}\in\mathbb{R}^2,\omega^*\in\mathbb{S}^1} K(\mathbf{y}-\mathbf{x})\omega^* f(\mathbf{y},\omega^*)\, d\mathbf{y}\mathrm{d}\omega^*, \tag{2.6}$$

with K the characteristic function of the ball $B(0,R)$, i.e. $K(r) = \mathbb{1}_{\{|r|<R\}}$.

In the large scale limit in space and time (see section 2.3), the vector velocity $F(f)$ becomes *local* in space meaning that J is given by:

$$J(\mathbf{x}) = \int_{\omega^*\in\mathbb{S}^1} \omega^* f(\mathbf{x},\omega^*)\, \mathrm{d}\omega^*. \tag{2.7}$$

This non-linear kinetic model (2.4)-(2.5) for orientational interactions, with the constitutive mean flux relation $J(\mathbf{x})$ given by, either a global form (2.6) for an integrable kernel $K(r)$, or the local form (2.7), was shown in [24] to have non-negative global weak solution in $C(0,T;L^1(D)\cap L^\infty((0,T)\times D))$ with $D=\mathbb{R}^d\times\mathbb{S}^{d-1}$, for any time T, with non-negative initial data $f_0\in(L^1\cap L^\infty)(D)$, under the assumption that the constitutive mean flux relation $J(\mathbf{x})$ does not vanish at any time $t\in[0,T]$. In addition, the following estimates for the solution f hold for any $1\le p<\infty$,

$$\|f\|_{L^\infty(0,T;L^p(D))} + \frac{2\sigma(p-1)}{p}\|\nabla_\omega f^{\frac{p}{2}}\|^{\frac{2}{p}}_{L^2((0,T)\times D)} \le e^{CT\frac{p}{p-1}}\|f_0\|_{L^p(D)}, \tag{2.8}$$

and

$$\|f\|_{L^\infty((0,T)\times D)} \le e^{CT}\|f_0\|_{L^\infty(D)}. \tag{2.9}$$

These estimates are significant for the analysis of the numerical scheme proposed in the following section. While this analysis will not be carried out in the present manuscript, we anticipate that convergence and error estimates recently obtained in [1] for these type of spectral conservative schemes developed for the case of classical Boltzmann dynamics for binary interactions in [21–23], may also apply to our approximation presented next, in section 3.

In the following, we only consider $J(\mathbf{x})$ within the approximation (2.7). We rewrite the kinetic equation (2.4) in the following form:

$$\partial_t f + \omega\cdot\nabla_{\mathbf{x}} f = Q(f), \tag{2.10}$$

with Q the collisional operator given by:

$$Q(f) = -\nabla_\omega\cdot(F[f]f) + \sigma\Delta_\omega f, \tag{2.11}$$

with $F(f)$ given by (2.5),(2.7).

2.3 Macroscopic model (hydrodynamic limit)

In order to derive a macroscopic model associated with the kinetic model (2.4), one has to introduce an hydrodynamic scaling [16] introducing the macroscopic variables:

$$t' = \varepsilon t \quad , \quad x' = \varepsilon x,$$

where ε is the ratio between *micro* and *macro* variables. In these new *macro* variables, the evolution of f^ε is given by:

$$\partial_t f^\varepsilon + \omega \cdot \nabla_{\mathbf{x}} f^\varepsilon = \frac{1}{\varepsilon} Q(f^\varepsilon). \tag{2.12}$$

As $\varepsilon \to 0$, one can show that the evolution f^ε converges locally in space toward an *equilibrium* (see subsection 3.1):

$$f^\varepsilon \rightharpoonup f^0(x,\omega) = \rho^0(x) M_{u(x)}(\omega). \tag{2.13}$$

The evolution of the system is solely described by two macroscopic quantities: the density of particles ρ and the macroscopic velocity u. Their evolutions are governed by the following system:

$$\partial_t \rho + \nabla_x \cdot (c_1 \rho u) = 0, \tag{2.14}$$
$$\rho \Big(\partial_t u + c_2 (u \cdot \nabla_x) u \Big) + \lambda \, P_{u^\perp} \nabla_x \rho = 0, \tag{2.15}$$
$$|u| = 1. \tag{2.16}$$

Here, c_1, c_2 and λ are constants depending on the noise parameter σ, $P_{u^\perp}$ is a projection operator given by $P_{u^\perp} = (\mathrm{Id} - u \otimes u)$. It ensures the constraint that $|u| = 1$. The macroscopic model is a hyperbolic system but it is also non-conservative. Thus, few analytic results are known about this system. Local existence and uniqueness have been studied in [15] and we refer to [31] for the implementation of an accurate numerical scheme.

3 Numerical scheme for the kinetic model

We turn our attention on building a numerical scheme for the kinetic model (2.10) in 2D. With this aim, we propose a splitting method between the collision and the transport part of the equation. In other words, we solve separately:

$$\partial_t f = Q(f) \tag{3.1}$$
$$\partial_t f + \omega \cdot \nabla_x f = 0. \tag{3.2}$$

The difficulty is essentially in the collisional part (3.1), it requires to use wisely the properties of Q (Subsection 3.1). We propose a spectral method (subsection 3.2) that preserves the invariants of Q (Subsection 3.3). Next, we use a finite volume method to solve the transport term (3.2) (Subsection 3.4). A summary of the proposed numerical scheme is given in A.

3.1 Properties of the collisional operator

The collisional operator (2.11) can be written as a Fokker-Planck operator. To do so, we introduce the equilibrium function $M_\Omega(\omega)$, also known as the Von Mises distribution,

$$M_\Omega(\omega) = C_0 \exp\left(\frac{\omega \cdot \Omega}{\sigma}\right), \tag{3.3}$$

where C_0 is a constant of normalization. In 2D, this gives the formula:

$$M_{\overline{\theta}}(\theta) = C_0 \mathrm{e}^{\dfrac{\cos(\theta - \overline{\theta})}{\sigma}} \tag{3.4}$$

with $\Omega = (\cos\overline{\theta}, \sin\overline{\theta})$.

Proposition 3.1 *Let $\Omega_f \in \mathbb{S}^1$ be the direction of the average velocity of f $\Big($i.e. $\Omega_f = \frac{\int_\omega f\omega\,\mathrm{d}\omega}{|\int_\omega f\omega\,\mathrm{d}\omega|}\Big)$. We have*

$$Q(f) = \sigma \nabla_\omega \cdot \left(M_{\Omega_f} \nabla_\omega \Big(\frac{f}{M_{\Omega_f}}\Big)\right). \tag{3.5}$$

In particular,

$$\int_{\omega\in\mathbb{S}^1} Q(f) f \frac{\mathrm{d}\omega}{M_{\Omega_f}} = -\sigma \int_{\omega\in\mathbb{S}^1} M_{\Omega_f} \left| \nabla_\omega \Big(\frac{f}{M_{\Omega_f}}\Big)\right|^2 \mathrm{d}\omega \leq 0.$$

In 2D, equation (3.5) reads:

$$Q(f) = \sigma\partial_\theta \left(M_{\overline{\theta}}\, \partial_\theta \left(\frac{f}{M_{\overline{\theta}}}\right)\right) = -\partial_\theta \Big(\sin(\overline{\theta} - \theta) f\Big) + \sigma \partial_\theta^2 f. \tag{3.6}$$

Corollary 3.2 *The equilibria of the operator Q are given by the set:*

$$\mathcal{E} = \{\rho M_\Omega \mid \rho \in \mathbb{R}\ ,\ \Omega \in \mathbb{S}^1\}. \tag{3.7}$$

Although the equilibria of the operator Q forms a set of dimension d (1 for ρ and $d-1$ for Ω), the collisional invariants of Q are only of dimension 1. In particular, Q preserves only the mass and not the flux. In other words, for a general f, we have:

$$\int_{\omega\in\mathbb{S}^1} Q(f)\,\mathrm{d}\omega = 0 \qquad \text{and} \qquad \int_{\omega\in\mathbb{S}^1} Q(f)\omega\,\mathrm{d}\omega \neq 0.$$

To overcome the lack of conservations of Q, we generalize the notion of collisional invariant.

Definition 1 (GCI) *Fix a unit vector Ω. A function ψ_Ω is called a generalized collisional invariant (GCI) if it satisfies:*

$$\int_{\omega\in\mathbb{S}^1} Q(f)\psi_\Omega(\omega)\,\mathrm{d}\omega = 0, \tag{3.8}$$

for any f satisfying $\Omega_f = \pm\Omega$.

Once we fix the direction Ω_f, the operator Q becomes linear in f. We denote by Q_Ω the linear operator defined by:

$$Q_\Omega(f) = \sigma\nabla_\omega \cdot \left(M_\Omega\nabla_\omega\Big(\frac{f}{M_\Omega}\Big)\right).$$

Thus, we can define the adjoint of Q_Ω in L^2:

$$Q^*_\Omega(\varphi) = \sigma M_\Omega^{-1}\nabla_\omega \cdot (M_\Omega\,\nabla_\omega\varphi)\,. \tag{3.9}$$

Expressing the constraint $\Omega_f = \Omega$ as a Lagrange multiplier, we find that ψ_Ω is a collisional invariant for Ω if and only if it satisfies:

$$Q^*_\Omega(\psi_\Omega) = \beta\omega\times\Omega$$

with $\beta\in\mathbb{R}$. We deduce an explicit expression for ψ_Ω in 2D.

From now on, we omit the subindex Ω in the notation of the Von Misses distribution, that is $M := M_\Omega$.

Proposition 3.3 *In 2D, suppose that $\Omega = (1,0)^T$. The collisional invariants ψ satisfy:*

$$\sigma\partial_\theta(M\partial_\theta\psi) = \beta\sin\theta M,$$

with $M(\theta) = C_0\exp\left(\frac{\cos\theta}{\sigma}\right)$. Thus, the solution corresponding to $\beta = 1$ is given by:

$$\psi(\theta) = \sigma\theta - \sigma\pi\frac{\int_0^\theta \mathrm{e}^{-\frac{\cos s}{\sigma}}\,\mathrm{d}s}{\int_0^\pi \mathrm{e}^{-\frac{\cos s}{\sigma}}\,\mathrm{d}s}. \tag{3.10}$$

For Ω given by $\Omega = (\cos\overline{\theta}, \sin\overline{\theta})^T$, a solution is written as

$$\psi_\Omega(\theta) = \psi(\theta - \overline{\theta}). \tag{3.11}$$

3.2 Spectral method

In the section, we introduce a Hilbert space to decompose the collisional operator. In the following, we are looking at the equation (3.1) *locally* in $\mathbf{x}$. For clarity, we suppose that $\Omega(\mathbf{x})$ is given by the vector $(1,0)^T$, the result for more general Ω can be found through rotation of this solution. We introduce the subspace of periodic functions H defined as:

$$H := \{f(\theta) \;/\; \int_0^{2\pi} |f(\theta)|^2 \frac{\mathrm{d}\theta}{M(\theta)} < \infty\}, \tag{3.12}$$

along with the scalar product $\langle , \rangle_H$:

$$\langle f,\, g\rangle_H := \int_0^{2\pi} f(\theta) g(\theta) \frac{\mathrm{d}\theta}{M(\theta)}.$$

The relevance of this scalar product comes from the symmetric property satisfied by Q: suppose f, g are smooth functions of H, then

$$\langle Q(f), g\rangle_H = -\sigma \int_0^{2\pi} M \partial_\theta\left(\frac{f}{M}\right)\, \partial_\theta\left(\frac{g}{M}\right)\, \mathrm{d}\theta = \langle f, Q(g)\rangle_H.$$

As a Hilbert basis on H, we use the following functions:

$$P_k(\theta) = \mathrm{e}^{ik\theta}\sqrt{\frac{M(\theta)}{2\pi}}, \quad k \in \mathbb{Z}. \tag{3.13}$$

Using the formulation (3.6), we deduce that:

$$Q(P_k) = \left(-\sigma k^2 + \frac{\cos\theta}{2} - \frac{\sin^2\theta}{4\sigma}\right) P_k. \tag{3.14}$$

Thus,

$$Q(P_k) = \frac{1}{16\sigma} P_{k-2} \;+\; \frac{1}{4} P_{k-1} \;+\; \left(-\sigma k^2 - \frac{1}{8\sigma}\right) P_k \;+\; \frac{1}{4} P_{k+1} \;+\; \frac{1}{16\sigma} P_{k+2}.$$

For any function f in H, we can decompose:

$$f(\theta) = \sum_{k\in\mathbb{Z}} c_k P_k(\theta) \quad , \quad \text{with } c_k = \langle f,\, P_k\rangle_H.$$

and deduce that $Q(f) = \sum_{k\in\mathbb{Z}} \widetilde{c}_k P_k(\theta)$ with

$$\widetilde{c}_k = \frac{1}{16\sigma} c_{k-2} \;+\; \frac{1}{4} c_{k-1} \;+\; \left(-\sigma k^2 - \frac{1}{8\sigma}\right) c_k \;+\; \frac{1}{4} c_{k+1} \;+\; \frac{1}{16\sigma} c_{k+2}.$$

Numerically, we use a uniform grid to divide the domain $[0, 2\pi)$ in $2N$ points: $\theta_s = s\Delta\theta$ with $\Delta\theta = \frac{2\pi}{2N}$. We approximate the Hilbert space H (3.12) by a subspace of finite dimension:

$$V_N = \{f_N(\theta) = \sum_{k=-N}^{N} c_k P_k(\theta), \quad \text{with } c_{-N}, \ldots, c_N \in \mathbb{C}\}. \tag{3.15}$$

Notice that on the grid point θ_s, we have $P_k(\theta_s) = P_{k+2N}(\theta_s)$. Thus, only $2N+1$ polynomials P_K are relevant. For a given function f in H, we define its approximation f_N in V with coefficients c_k given by:

$$c_k = \sum_{s=0}^{2N-1} f(\theta_s)\overline{P}_k(\theta_s)\frac{\Delta\theta}{M(\theta_s)}. \tag{3.16}$$

Similarly to the Discrete Fourier Transform, the function f_N interpolates f at the grid points θ_s. By periodicity and using that f is a real function, we deduce that (see figure 1):

$$c_k = c_{k+2N} \quad , \quad c_{-k} = \overline{c}_k. \tag{3.17}$$

Therefore, only the coefficients $c_0, \ldots, c_N$ are required to describe f_N.

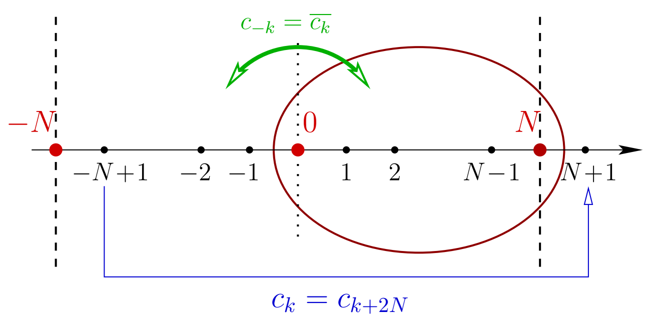

Figure 1: The coefficients $\{c_k\}_k$ (3.16) satisfy the properties $c_k = c_{k+2N}$ and $c_{-k} = \overline{c_k}$. Thus, only the coefficients c_k from 0 to N are needed.

Applying the operator Q to the approximation f_N gives:

$$Q(f_N) = \sum_{k=-N..N} c_k\Big[\alpha_2 P_{k-2} + \alpha_1 P_{k-1} + (-\sigma k^2 - \alpha_0)P_k + \alpha_1 P_{k+1} + \alpha_2 P_{k+2}\Big], \tag{3.18}$$

with $\alpha_0 = \frac{1}{8\sigma}$, $\alpha_1 = \frac{1}{4}$, $\alpha_2 = \frac{1}{16\sigma}$. Since $P_{k+2N}(\theta_s) = P_k(\theta_s)$, we deduce that Q has the following matrix representation in the basis $\mathcal{B} = \{P_k\}_{-N \le k \le N}$ of V_N:

$$
[Q]_{\mathcal{B}} = \left[\begin{array}{ccccccccc}
-\sigma N^2 - \alpha_0 & \alpha_1 & \alpha_2 & & 0 & & & \alpha_2 & \alpha_1 \\
 & & & & & & & & \alpha_2 \\
 & \ddots & \ddots & \ddots & \ddots & \ddots & & & \\
0 & & \alpha_2 & \alpha_1 & -\sigma k^2 - \alpha_0 & \alpha_1 & \alpha_2 & & 0 \\
 & & & \ddots & \ddots & \ddots & \ddots & \ddots & \\
\alpha_1 & & & & & & & & \\
\alpha_2 & \alpha_1 & & & 0 & & \alpha_2 & \alpha_1 & -\sigma N^2 - \alpha_0
\end{array} \right]. \tag{3.19}
$$

3.3 Time discretization

We now propose a numerical scheme to solve the collision operator (3.1). We denote by $\mathbf{c} = (c_{-N}, \dots, c_N)^T$ the coefficients (3.16). In the subspace V_N, the equation (3.1) reduces to:

$$\partial_t \mathbf{c} = [Q]_{\mathcal{B}} \mathbf{c}. \tag{3.20}$$

We would like to find a discretization of this system that preserves the collisional invariants of f (see 3.1). In other words, if f^{n+1} is the update of f^n, we should have:

$$\int_0^{2\pi} f^n \begin{pmatrix} 1 \\ \psi \end{pmatrix} \mathrm{d}\theta = \int_0^{2\pi} f^{n+1} \begin{pmatrix} 1 \\ \psi \end{pmatrix} \mathrm{d}\theta, \tag{3.21}$$

which leads to:

$$\mathcal{C}\mathbf{c^{n+1}} = \mathcal{C}\mathbf{c^n} \tag{3.22}$$

where $\mathbf{c^n}$ and $\mathbf{c^{n+1}}$ are (resp.) the coefficients of f^n and f^{n+1}, and $\mathcal{C}$ is a $2 \times (2N+1)$ matrix defined by:

$$\mathcal{C}_{0,k} = \int_0^{2\pi} P_k(\theta)\, \mathrm{d}\theta \quad , \quad \mathcal{C}_{1,k} = \int_0^{2\pi} P_k(\theta)\psi(\theta)\, \mathrm{d}\theta \quad \text{ for all } k \in [\![-N, N]\!].$$

The algorithm we propose consists in solving (3.20) using an Euler scheme and to project the solution obtained to satisfy the constraint (3.22). In other words, we write:

$$\mathbf{c}^* = \mathbf{c}^n + \Delta t [Q]_{\mathcal{B}} \mathbf{c}^n. \tag{3.23}$$

and then compute $\mathbf{c}^{n+1}$ such that the constraint (3.22) is satisfied with $\|\mathbf{c}^{n+1} - \mathbf{c}^n\|_H$ minimized (see figure 2).

Following [21], we obtain the following algorithm:

Proposition 3.4 *The coefficients $\mathbf{c^{n+1}}$ are given by:*

$$\mathbf{c^{n+1}} = \mathbf{c^n} + \Delta t \Lambda_N(\mathcal{C})\, [Q]_{\mathcal{B}}\, \mathbf{c^n}, \tag{3.24}$$

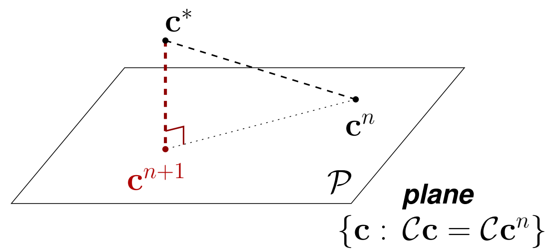

Figure 2: The update coefficients $\mathbf{c}^{n+1}$ has to (i) belong to the *invariant plane* $\mathcal{P} = \{\mathbf{c} : \mathcal{C}\mathbf{c} = \mathcal{C}\mathbf{c}^{\mathbf{n}}\}$ and (ii) minimize the distance with the auxiliary estimation $\mathbf{c}^*$. Therefore, $\mathbf{c}^{n+1}$ has to be taken as the orthogonal projection of $\mathbf{c}^*$ on the plane $\mathcal{P}$.

with $\Lambda_N(\mathcal{C})$ the square matrix defined as:

$$\Lambda_N(\mathcal{C}) = Id - \mathcal{C}^T\left(\mathcal{C}\mathcal{C}^T\right)^{-1}\mathcal{C}. \tag{3.25}$$

Numerically, the *explicit* Euler scheme (3.23) could be unstable due to the stability condition (i.e. $\frac{\sigma}{4}N^2\Delta t \lesssim 1$, see B). Thus, we propose a second algorithm based on the *implicit* Euler scheme:

$$\mathbf{c}^*_{\mathbf{k}} = \mathbf{c}^{\mathbf{n}}_{\mathbf{k}} + \Delta t\,[Q]_{\mathcal{B}}\,\mathbf{c}^*_{\mathbf{k}}. \tag{3.26}$$

Following the same methodology, we deduce the following algorithm:

$$\mathbf{c}^{\mathbf{n+1}} = \mathbf{c}^{\mathbf{n}} + \Delta t\Lambda_N(\mathcal{C})\,[Q]_{\mathcal{B}}\,(\mathrm{Id} - \Delta t\,[Q]_{\mathcal{B}})^{-1}\mathbf{c}^{\mathbf{n}}, \tag{3.27}$$

with $\Lambda_N(\mathcal{C})$ the square matrix given by (3.25). Notice that the *implicit* scheme requires to estimate the matrix $(\mathrm{Id} - \Delta t\,[Q]_{\mathcal{B}})^{-1}$. The matrix inversion has to be computed only once as $[Q]_{\mathcal{B}}$ is independent of the cells and time.

3.4 Transport term

Finally, we propose a finite volume method [28] to solve the transport equation (3.2).

Suppose f is defined on a Cartesian grid in (x,y), $f(x_i,y_j,\theta)$. The finite volume method consists of identifying $f(x_i,y_j,\theta)$ as the mass of particles in the cell $\mathcal{C}_{i,j} = [x_{i-\frac12},x_{i+\frac12}]\times[y_{j-\frac12},y_{j+\frac12}]$ moving with speed $\omega(\theta) = (\cos\theta, \sin\theta)$. Integrating the transport equation on the cell $\mathcal{C}_{i,j}$ yields

$$\begin{aligned}\frac{d}{dt}f(x_i,y_j) \;+\; \cos\theta\,\frac{f(x_{i+\frac12},y_j) - f(x_{i-\frac12},y_j)}{\Delta x}& \\ +\;\sin\theta\,\frac{f(x_i,y_{j+\frac12}) - f(x_i,y_{j-\frac12})}{\Delta y}&\; = 0.\end{aligned} \tag{3.28}$$

It remains to determine the values of the interface of the cell $\mathcal{C}_{i,j}$ (e.g. $f(x_{i+\frac{1}{2}}, y_j, \theta)$, $f(x_i, y_{j+\frac{1}{2}}, \theta)$). We use an upwind approach: for each value of θ, the value of f at the boundary is given by:

$$f(x_{i+\frac{1}{2}}, y_j, \theta) = \begin{cases} f(x_i, y_j, \theta) & \text{if } \cos\theta \geq 0 \\ f(x_{i+1}, y_j, \theta) & \text{if } \cos\theta < 0. \end{cases} \tag{3.29}$$

The stability condition for this algorithm is $c_{max}\Delta t < \Delta x$ where c_{max} is the maximum speed at which f is transported. Since $|\omega| \leq 1$, we enforce numerically that $\Delta t < \Delta x$.

4 Numerical investigations

Using the numerical scheme developed for the kinetic equation (2.10), we now investigate the Vicsek model using either its particle description (2.1), kinetic formulation (2.10), or hydrodynamic limit (2.14)-(2.15).

We first validate our numerical scheme for the kinetic equation by solving the homogeneous equation (3.1) and analyzing its convergence toward equilibrium (2.13). In particular, we highlight the importance of preserving the invariants for the stability of large time simulation. Next, we investigate the kinetic equation within its hydrodynamic limit, i.e. letting $\varepsilon \to 0$ in (2.12). Our results show that at $\varepsilon = 10^{-2}$ the solutions of the kinetic equation and the hydrodynamic limit are almost indistinguishable. For instance, we recover at the kinetic level shock and rarefaction waves. Finally, we explore the effect of boundary conditions on the dynamics. We use a domain with reflexive boundary conditions and compare the solution of the particle dynamics with the kinetic formulation once they reach a stationary state.

In all the simulations, we use the *implicit* scheme (3.27) to solve the collisional operator. The results are similar with the *explicit* scheme (3.23) but requires an additional constraint on the time step Δt for the stability of the scheme (see B). In term of CPU time, both methods gives analogous results. The intensity of the noise is fixed at $\sigma = .2$ for the three descriptions of the system (*micro/kinetic/macro*).

4.1 Convergence to equilibrium

In this subsection, we validate our numerical scheme for the kinetic equation using analytic results. Since the stationary states of the homogeneous equation are known, we can test that our scheme converges toward such analytic solutions.

With this aim, we use our numerical scheme to solve the homogeneous equation $\partial_t f = Q(f)$ with Q defined in (2.11). We use as initial condition a sinusoid for $f(\theta)$

$$f(t=0, \theta) = 1 + \cos 2\theta.$$

We leave the discussion about the time and velocity discretization (Δt and $\Delta\theta$) of the kinetic equation in B and we discuss in C the accuracy of the scheme. In figure 3, we plot the solution $f(t)$ at $t = 10$ unit times and the corresponding stationary state (i.e. Von Mises distribution (3.3)). We observe that the two curves are in perfect agreement.

The mean direction $\overline{\theta}$ of $f(t,\theta)$ can vary during a simulation. This is expected since the mean velocity is not conserved by the kinetic equation (2.10). However, the total mass, $\rho(t) = \int_0^{2\pi} f(t,\theta)\,\mathrm{d}\theta$, has to be conserved in time. Thanks to our formulation (3.24), the mass is precisely conserved in our simulation (up to round-off error). If one would use the formulation (3.23) to update f (i.e. without the constraint), one cannot guarantee that the mass would be preserved. To analyze this property, we numerically investigate the long time behavior of the mass $\rho(t)$ with and without taking into account the invariant of the dynamics. Thus, we use a *preserving* and a *non-preserving* scheme. In figure 4, we represent the evolution of the total mass $\rho(t)$ in time for both cases. With the preserving scheme, the mass $\rho(t)$ remains constant over time whereas the mass $\rho(t)$ is increasing with the non-preserving scheme which is inaccurate.

4.2 Traveling waves

We now turn our attention to the full kinetic equation (2.4). Few analytic results are known for this equation other than hydrodynamic limit. Therefore, we will numerically investigate the kinetic equation in the hydrodynamic regime, i.e., we investigate the solution of (2.12) for small value of ε and compare it with the solution of the hydrodynamic model (2.14)-(2.15).

To compare the solution f^ε of the kinetic equation (2.12) and the solution (ρ, u) of the hydrodynamic limit (2.14)-(2.15), we analyze the evolution of the two first moments of f^ε corresponding to the mass ρ^ε and the macroscopic velocity u^ε. They are obtained through averaging of f^ε in velocity variables:

$$\rho^\varepsilon(x) = \int_0^{2\pi} f^\varepsilon(x,\theta)\,\mathrm{d}\theta\ ,\ u^\varepsilon(x) = \frac{j^\varepsilon(x)}{|j^\varepsilon(x)|} \ \text{ with } \ j^\varepsilon(x) = \int_0^{2\pi} \begin{pmatrix}\cos\theta\\ \sin\theta\end{pmatrix} f^\varepsilon(x,\theta)\,\mathrm{d}\theta.$$

Both quantities ρ^ε and u^ε are expected to converge to the solution of the hydrodynamic system (2.14)-(2.15) as $\varepsilon \to 0$. Thus, we compute the solutions of the kinetic equation (2.12) with different ε (resp. $\varepsilon \in \{1, 10^{-1}, 10^{-2}\}$). The hydrodynamic system (2.14)-(2.15) plays the role of a benchmark in this approach.

To obtain interesting patterns, we use as an initial condition a Riemann problem in the x-direction and we suppose that the solution is homogeneous in the y-direction. Thus, for the hydrodynamic limit, the initial condition is prescribed by two values (ρ_l, u_l) and (ρ_r, u_r) corresponding to the values at the left and right

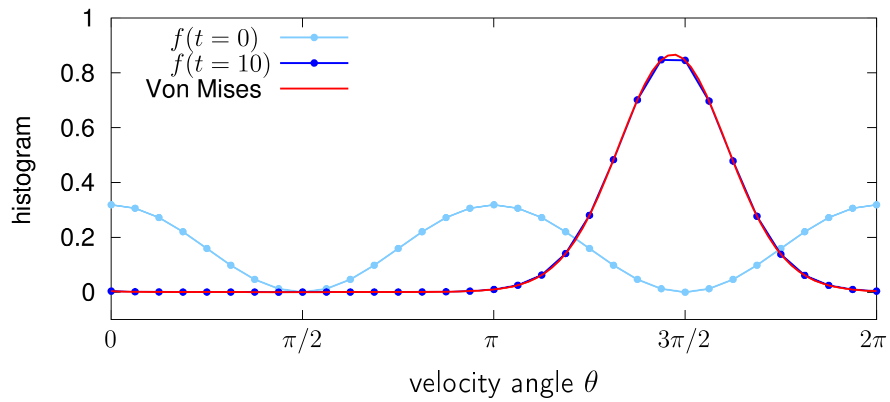

Figure 3: Solution of the homogeneous equation $\partial_t f = Q(f)$. The solution $f(t,\theta)$ (blue) converges to an equilibrium (red) given by a Von Mises distribution. Parameters for the simulation: $\sigma = .2$, $\Delta t = .05$, $\Delta\theta = \frac{2\pi}{32}$.

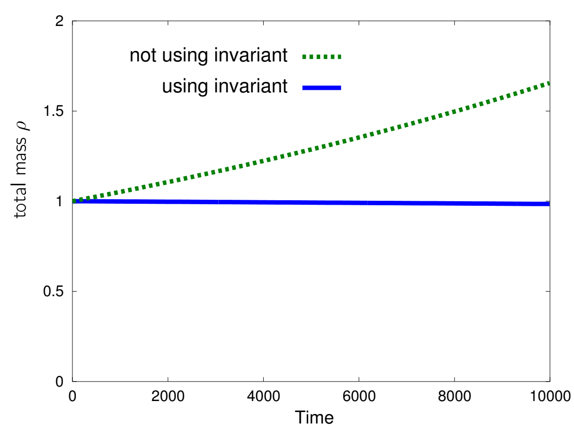

Figure 4: Evolution of the total mass $\rho = \int_0^{2\pi} f(\theta)\,\mathrm{d}\theta$ for the homogeneous equation with and without implementing the constraint (3.21). We observe that the mass increases if we do not enforce the constraint. Parameters for the simulation: $\sigma = .2$, $\Delta t = .1$, $\Delta\theta = \frac{2\pi}{12}$.

side of the domain (resp.). For the kinetic equation, we suppose that f^ε starts from local equilibrium meaning that $f^\varepsilon(x,\theta)$ is initially a Von Mises distribution for any x. For the two remaining degrees of freedom, ρ^ε and $\overline{\theta}^\varepsilon$, we initiate them such that the moments of f^ε match with the initial condition of the hydrodynamic limit.

We investigate three different Riemann problems. For our first simulation, the solution of the macroscopic model is given by a rarefaction wave:

$$(\rho_l,\theta_l) = (2, 1.7)\ , \qquad (\rho_r,\theta_r) = (0.218, 0.5). \tag{4.1}$$

In figure 5, we represent the density $\rho^\varepsilon(x)$ and angle velocity $\theta^\varepsilon(x)$ at $t = 4$ unit time. We do observe that, as $\varepsilon \to 0$, the solution given by the kinetic equation $(\rho^\varepsilon, \theta^\varepsilon)$ gets closer and closer to the solution of the hydrodynamic model (ρ, u). The effect of ε can be seen as a "smoothing parameter". It is consistent with the derivation of the hydrodynamic limit where the second order approximation in ε gives a diffusion-type operator [17].

For our second simulation, we use a Riemann problem that generates a shock solution. We use for that the initial condition:

$$(\rho_l,\theta_l) = (1, 1.5)\ , \qquad (\rho_r,\theta_r) = (2, 1.83). \tag{4.2}$$

We plot the solutions of both the kinetic equation and hydrodynamic limit at time $t = 4$ unit time in figure 6. Once again, the moments $(\rho^\varepsilon, u^\varepsilon)$ do converge toward the shock profile given by the solution of the hydrodynamic model (ρ, u). We note that there is no analytic solution for the shock wave since the hydrodynamic model is not conservative, we lack the Rankine-Hugoniot conditions to find an explicit value for the shock speed. Hence, it is quite remarkable that both the kinetic formulation and the hydrodynamic model give the same shock profile with the same speed.

An additional inspection of the solutions suggest that the solution of the kinetic model might present cusp formation. For instance, in figure 5 (right), we observe a 'blob' forming at $x \approx 3.7$ unit space, that vanishes as $\varepsilon \to 0$. There is a similar but 'more disperse' pattern in the figure 6 at $x \approx 1$ unit space. The formation of cusps will have a strong importance for the understanding of the kinetic model.

For our third simulation, the Riemann problem used is a contact discontinuity (see figure 7):

$$(\rho_l,\theta_l) = (1, 1)\ , \qquad (\rho_r,\theta_r) = (1, -1). \tag{4.3}$$

Here, the solution of the hydrodynamic model is more complex than a rarefaction wave or a shock wave. As for the shock profile (figure 6), there is no analytic expression for this solution. But once again, the solution given by the kinetic equation does converge as $\varepsilon \to 0$ toward the complex profile of the hydrodynamic model. Thus, these numerical simulations at the kinetic level confirm the relevance of the profile observed at the macroscopic level.

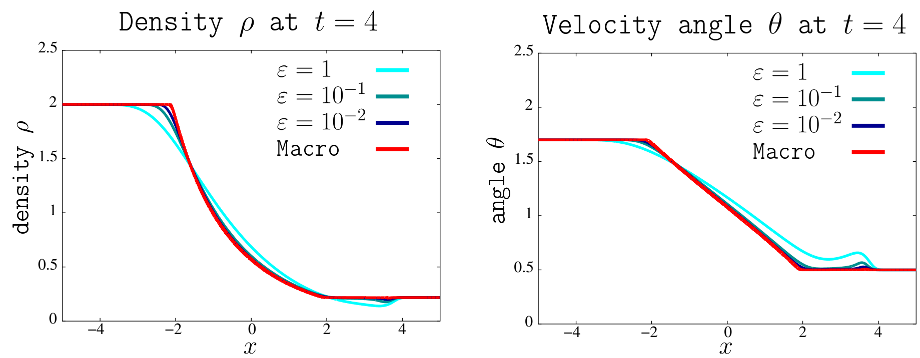

Figure 5: The solutions of the Riemann problem (4.1) is given by a rarefaction wave. **Left**: the mass ρ^ε for the kinetic equation (blue) and for the hydrodynamic model (red). **Right**: the velocity angle θ^ε for the kinetic equation (blue) and for the hydrodynamic model (red).

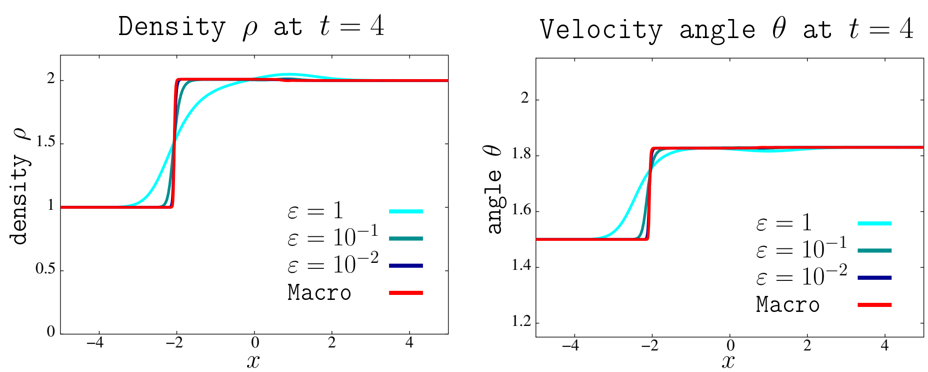

Figure 6: Shock wave solution of the Riemann problem (4.2).

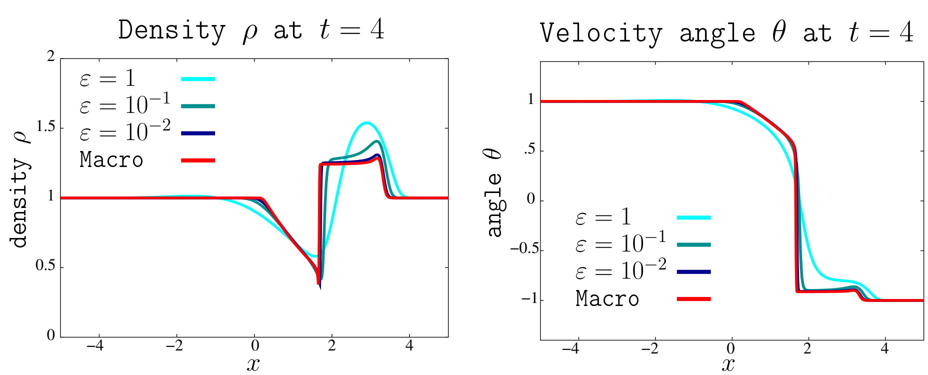

Figure 7: Contact discontinuity solution of the Riemann problem (4.3).

4.3 Vortex formation

In all the previous simulations, we have used Neumann boundary conditions in order to reduce the influence of the boundary of the domain on the dynamics. We would like now to investigate in more details the impact of boundary conditions on the dynamics. For this purpose, we compare the kinetic model (2.4) and the microscopic model (2.1) in a bounded domain Ω with reflexive boundary conditions. At the microscopic level, each time a particle i hits the boundary (*i.e.* $x_i \in \partial\Omega$), its velocity ω_i is *reflected*:

$$\widehat{\omega}_i = S_{\partial\Omega(x)}(\omega_i) = \omega_i - 2\langle \omega_i, \eta\rangle \eta$$

where η is the unit normal vector at $\partial\Omega(x)$ (see figure 8). Similarly, at the kinetic level, reflexive boundary conditions impose that f satisfies at the boundary:

$$f(x,\omega) = f(x, S_{\partial\Omega(x)}(\omega)) \qquad \text{for } \ x \in \partial\Omega.$$

In other words, we have no-flux boundary conditions. In contrast to the kinetic model, reflexive boundary conditions would be more delicate to implement for the hydrodynamic model due to the constraint $|u| = 1$. Moreover, the validity of the hydrodynamic model near the boundary is questionable due to the possible formation of boundary layers (e.g. Prandtl's boundary layer).

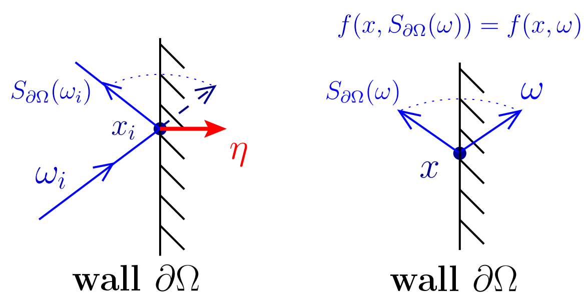

Figure 8: **Left:** Reflexive boundary conditions for the particle model. Once x_i reaches the boundary $\partial\Omega$, its velocity ω_i is reflected. **Right:** Reflexive boundary conditions for the kinetic model: outgoing flux (i.e. $f(x,\omega)$) equals the incoming flux (i.e. $f(x, S_{\partial\Omega}(\omega))$) at the boundary $x \in \partial\Omega$ in all direction ω.

Starting from a uniform distribution in space and velocity, we run the Vicsek model for both the particle and kinetic level. Both simulations are run on a square domain Ω of 10 space units. For the particle level, we perform three runs with respectively $5 \cdot 10^3$, 10^4 and $5 \cdot 10^4$ particles with a radius of interaction $R = .2$ and a time discretization of $\Delta t = .01$ unit time. For the kinetic model, we use a mesh grid $\Delta x = \Delta y = .2$ and a larger time discretization $\Delta t = .05$ to reduce the numerical viscosity. We use 32 modes to discretize the velocity distribution.

After a transient period, both simulations converge toward a stationary state consisting of a vortex-type formation. In figure 9, we represent the spatial density ρ and macroscopic velocity $\mathbf{u}$ defined as:

$$\rho(x) = \int_0^{2\pi} f(x,\theta)\,\mathrm{d}\theta, \qquad \rho(x)\mathbf{u}(x) = \int_0^{2\pi} \omega(\theta) f(x,\theta)\,\mathrm{d}\theta,$$

with $\omega(\theta) = (\cos\theta,\, \sin\theta)^T$. As a result of the reflexive boundary conditions and the alignment interaction, the flow $\mathbf{u}$ tends to follow the boundary. Here, the flow $\mathbf{u}$ is turning clockwise but it is equally probable that it would turn counter-clockwise since the initial distribution is uniform in space and velocity.

We notice that the particle model has more fluctuations compared to the kinetic model as we could expect. For instance, the solution of the kinetic model is invariant under rotation of angle $\pi/2$ which is not the case in the particle model due to fluctuations. To measure the agreement and the discrepancy between the two spatial distributions, we introduce the distribution $\varphi(\ell)$ measuring the average density on the squares C_ℓ centered at the origin with radius ℓ:

$$C_\ell = \{(x,y) \in \mathbb{R}^2 \mid \max(|x|,|y|) = \ell\}.$$

In other words, $\varphi(\ell)$ is defined for $\ell > 0$ as:

$$\varphi(\ell) = \frac{1}{|C_\ell|}\int_{C_\ell} \rho\,\mathrm{d}s \;=\; \frac{1}{4\ell}\int_{\{\|(x,y)\|_\infty = \ell\}} \rho\,\mathrm{d}s. \tag{4.4}$$

We average over squares instead of circles to take into account the geometry of the domain Ω. As we observe in figure 10, the distributions $\varphi(\ell)$ for the particle and kinetic models agree very well with each other. We observe some discrepancy near $\ell \approx 0$ and $\ell \approx 5$ corresponding respectively to the center and the boundary of the domain Ω. As we increase the number of particles, the discrepancies tend to disappear.

Overall, the kinetic model provides a reliable description of the microscopic model without the fluctuations. Moreover, the computation time of the microscopic model would drastically increase as the number of particles n becomes larger. Whereas, for the kinetic model, the computation time remains exactly the same when we increase the density.

Additional numerical investigations are required to better understand the discrepancy between the two curves. Both curves should coincide as the number of particles n and the number of modes N are approaching infinity since both methods converge to the analytic kinetic solution.

A way to obtain a quantification of such error will be analyzed in future work. As the number of particles n increases, one could estimate the convergence of the particle model (2.1) by means of Wasserstein metrics [8,9]. Moreover, we anticipate that the convergence analysis of our spectral method with respect to the number of spectral modes N can be performed by adapting existing work on conservative spectral schemes [1, 21]. Thus, one could estimate the relation between the number of particles n and spectral modes N for the kinetic equation by measuring the order of accuracy of both methods with respect to the analytic kinetic solution.

5 Conclusion

We presented the first numerical method for a kinetic description of the Vicsek swarming model, which poses a unique challenge as there is a distribution dependent collision invariant to satisfy when computing the interaction term. The method used a spectral representation linked with a discrete constrained optimization to compute these interactions, and shows excellent agreement with the macroscopic equations when near that regime. The numerical results emphasize the importance of enforcing the collision invariants in the system. Future work will seek to extend this formulation to the three dimensional Vicsek equation, which has two Generalized Collisional Invariants instead of one. An important issue to be further developed is the study of effects due to more intricate boundary conditions that can model more advanced wall avoidance, such as birds swerving when approaching a wall. Another interesting application is using the kinetic equation to study the dynamics of the non-conservative macroscopic equations that arise from this model, in particular, the formation of cusps. Finally, numerical analysis for the proposed scheme will be developed. As mentioned earlier, we anticipate that the semi discrete error and convergence analysis as the number of spectral modes N grows large, as applied by [1] to the conservative spectral schemes for classical Boltzmann dynamics for binary interactions [21], may also work for the proposed approximation of orientational interactions in the present work.

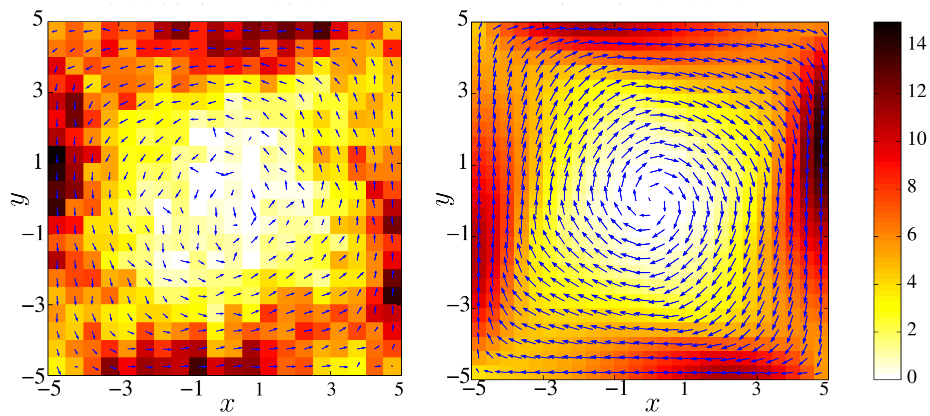

Figure 9: **Left**: density ρ and velocity $\mathbf{u}$ for the particle model (10^4 particles) at $t = 200$ unit time on a square domain with reflexive boundary conditions. **Right**: ρ and $\mathbf{u}$ for the kinetic model in for the same condition. Both solutions are close to a vortex-formation.

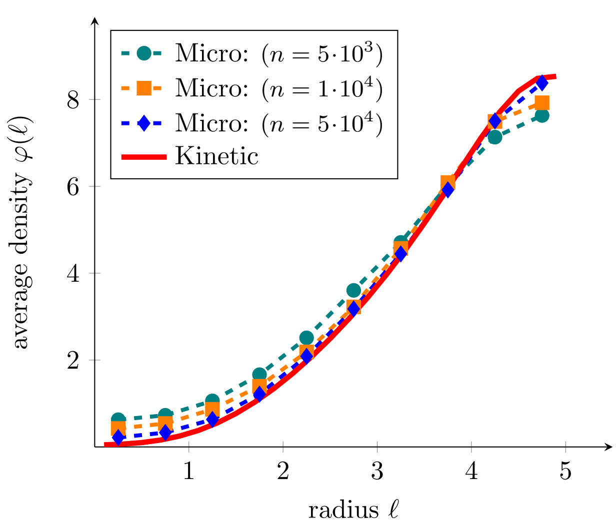

Figure 10: The average density $\varphi(\ell)$ (4.4) on the square C_ℓ for the particle model (dashed lines) and kinetic model (red) at time $t = 200$ (see figure 9). The distributions agree well with each other with some discrepancy at the origin ($\ell \approx 0$) and near the boundary of the domain ($\ell \approx 5$). The discrepancies reduce as the number of particles increases.

References

[1] R.J. Alonso, I. Gamba, and S.H. Tharkabhushanam. Convergence and error estimates of the Lagrangian based Conservative Spectral method for Boltzmann Equation. *Preprint*, 2014.

[2] I. Aoki. A simulation study on the schooling mechanism in fish. *Bulletin of the Japanese Society of Scientific Fisheries (Japan)*, 1982.

[3] M. Ballerini, N. Cabibbo, R. Candelier, A. Cavagna, E. Cisbani, I. Giardina, V. Lecomte, A. Orlandi, G. Parisi, and A. Procaccini. Interaction ruling animal collective behavior depends on topological rather than metric distance: Evidence from a field study. *Proceedings of the National Academy of Sciences*, 105(4):1232, 2008.

[4] G. A Bird. *Molecular gas dynamics and the direct simulation of gas flows.* Clarendon Press, 1994.

[5] A. V. Bobylev. The theory of the nonlinear spatially un1form Boltzmann equat1on for Maxwell molecules. *Mathematical physics reviews*, 7:111, 1988.

[6] A. V. Bobylev and S. Rjasanow. Difference scheme for the Boltzmann equation based on fast Fourier transform. *European Journal of Mechanics-B/Fluids*, 16(2):293–306, 1997.

[7] A. V. Bobylev and S. Rjasanow. Fast deterministic method of solving the Boltzmann equation for hard spheres. *European Journal of Mechanics-B/Fluids*, 18(5):869–887, 1999.

[8] F. Bolley, J. A. Cañizo, and J. A. Carrillo. Mean-field limit for the stochastic Vicsek model. *Applied Mathematics Letters*, 25(3):339–343, 2012.

[9] M. Bostan and J. A. Carrillo. Asymptotic fixed-speed reduced dynamics for kinetic equations in swarming. *Mathematical Models and Methods in Applied Sciences*, 23(13):2353–2393, 2013.

[10] J. Broadwell. Study of rarefied shear flow by the discrete velocity method. *J. Fluid Mech*, 19(3):401–414, 1964.

[11] C. Buet. A discrete-velocity scheme for the Boltzmann operator of rarefied gas dynamics. *Transport Theory and Statistical Physics*, 25(1):33–60, 1996.

[12] J. A. Cañizo, J. Carrillo, and J. Rosado. A well-posedness theory in measures for some kinetic models of collective motion. *Mathematical Models and Methods in Applied Sciences*, 21(03):515–539, 2011.

[13] Y. Chuang, M. R D'Orsogna, D. Marthaler, A. L Bertozzi, and L. S Chayes. State transitions and the continuum limit for a 2d interacting, self-propelled particle system. *Physica D: Nonlinear Phenomena*, 232(1):33–47, 2007.

[14] I. D Couzin, J. Krause, R. James, G. D Ruxton, and N. R Franks. Collective Memory and Spatial Sorting in Animal Groups. *Journal of Theoretical Biology*, 218(1):1–11, 2002.

[15] P. Degond, J. G. Liu, S. Motsch, and V. Panferov. Hydrodynamic models of self-organized dynamics: derivation and existence theory. *Methods and Applications of Analysis*, 20(2):89–114, 2013.

[16] P. Degond and S. Motsch. Continuum limit of self-driven particles with orientation interaction. *Mathematical Models and Methods in Applied Sciences*, 18(1):1193–1215, 2008.

[17] P. Degond and T. Yang. Diffusion in a continuum model of self-propelled particles with alignment interaction. *Mathematical Models and Methods in Applied Sciences*, 20(supp01):1459–1490, 2010.

[18] G. Dimarco and L. Pareschi. Numerical methods for kinetic equations. *Acta Numerica*, 23:369–520, 2014.

[19] F. Filbet and C. Mouhot. Analysis of spectral methods for the homogeneous Boltzmann equation. *Transactions of the American Mathematical Society*, 363(4):1947–1980, 2011.

[20] F. Filbet and L. Pareschi. A numerical method for the accurate solution of the Fokker-Planck-Landau equation in the nonhomogeneous case. *Journal of Computational Physics*, 179(1):1–26, 2002.

[21] I. Gamba and S. H. Tharkabhushanam. Spectral-Lagrangian methods for collisional models of non-equilibrium statistical states. *Journal of Computational Physics*, 228(6):2012–2036, 2009.

[22] I. Gamba and S. H. Tharkabhushanam. Shock and boundary structure formation by spectral-Lagrangian methods for the inhomogeneous Boltzmann transport equation. *J. Comput. Math*, 28(4):430–460, 2010.

[23] I. M. Gamba and J. R. Haack. A conservative spectral method for the Boltzmann equation with anisotropic scattering and the grazing collisions limit. *Journal of Computational Physics*, 270:40–57, 2014.

[24] Irene M. Gamba and Moon-Jin Kang. Global weak solutions for Kolmogorov-Vicsek type equations with orientational interaction. *arXiv preprint arXiv:1502.00293*, 2015.

[25] D. Goldstein, B. Sturtevant, and J. E. Broadwell. Investigations of the motion of discrete-velocity gases. *Progress in Astronautics and Aeronautics*, 117:100–117, 1989.

[26] S. Y Ha and E. Tadmor. From particle to kinetic and hydrodynamic descriptions of flocking. *Kinetic and Related Models*, 1(3):415–435, 2008.

[27] T. Inamuro and B. Sturtevant. Numerical study of discrete-velocity gases. *Physics of Fluids A: Fluid Dynamics (1989-1993)*, 2(12):2196–2203, 1990.

[28] R. J LeVeque. *Numerical Methods for Conservation Laws*. Birkhäuser, 1992.

[29] A. Mogilner and L. Edelstein-Keshet. A non-local model for a swarm. *Journal of Mathematical Biology*, 38(6):534–570, 1999.

[30] A. B. Morris, P. L. Varghese, and D. B. Goldstein. Monte Carlo solution of the Boltzmann equation via a discrete velocity model. *Journal of Computational Physics*, 230(4):1265–1280, 2011.

[31] S. Motsch and L. Navoret. Numerical simulations of a non-conservative hyperbolic system with geometric constraints describing swarming behavior. *Multiscale Modeling Simulation*, 9(3):1253–1275, 2011.

[32] L. Pareschi and B. Perthame. A Fourier spectral method for homogeneous Boltzmann equations. *Transport Theory and Statistical Physics*, 25(3-5):369–382, 1996.

[33] L. Pareschi and G. Russo. Numerical solution of the Boltzmann equation I: Spectrally accurate approximation of the collision operator. *SIAM journal on numerical analysis*, 37(4):1217–1245, 2000.

[34] L. Pareschi, G. Russo, and G. Toscani. Fast spectral methods for the Fokker-Planck-Landau collision operator. *Journal of Computational Physics*, 165(1):216–236, 2000.

[35] J. K Parrish, S. V Viscido, and D. Grunbaum. Self-organized fish schools: an examination of emergent properties. *Biological Bulletin, Marine Biological Laboratory, Woods Hole*, 202(3):296–305, 2002.

[36] C. W Reynolds. Flocks, herds and schools: A distributed behavioral model. In *ACM SIGGRAPH Computer Graphics*, volume 21, pages 25–34, 1987.

[37] F. Rogier and J. Schneider. A direct method for solving the Boltzmann equation. *Transport Theory and Statistical Physics*, 23(1-3):313–338, 1994.

[38] J. Toner and Y. Tu. Flocks, herds, and schools: A quantitative theory of flocking. *Physical Review E*, 58(4):4828–4858, 1998.

[39] C. M Topaz, A. L Bertozzi, and M. A Lewis. A Nonlocal Continuum Model for Biological Aggregation. *Bulletin of Mathematical Biology*, 68(7):1601–1623, 2006.

[40] T. Vicsek, A. Czirók, E. Ben-Jacob, I. Cohen, and O. Shochet. Novel type of phase transition in a system of self-driven particles. *Physical Review Letters*, 75(6):1226–1229, 1995.

A Summary of the numerical scheme

We summarize the different steps of the numerical scheme. We use the following notations: $x_i = i\Delta x$, $y_i = j\Delta y$, $\theta_s = s\Delta\theta$.

After the initialization of the distribution $f_{i,j,s} = f(x_i, y_j, \theta_s)$, the numerical scheme consists in iterating the following splitting method.

1) Collisional operator: in each cell (x_i, y_j)

   – *Decomposition*: compute the mean direction $\overline{\theta}$ and deduce $\{c_k\}_k$

$$c_k = \sum_s f(\theta_s + \overline{\theta}) P_{-k}(\theta_s) \frac{\Delta\theta}{M(\theta_s)}. \tag{A.1}$$

   – *Update*: $c_k^* = c_k + \Delta t \Lambda \widetilde{Q}(c_k)$.

   – *Reconstruct* f: $f_s = \sum_k c_k^* P_k(\theta_s - \overline{\theta})$.

2) Transport operator : for each velocity angle θ_s and in each case i, j

$$f_{i,j,s} = f_{i,j,s} - \frac{\Delta t \cos\theta_s}{\Delta x}(f_{i+\frac{1}{2},j,s} - f_{i-\frac{1}{2},j,s}) - \frac{\Delta t \sin\theta_s}{\Delta y}(f_{i,j+\frac{1}{2},s} - f_{i,j-\frac{1}{2},s}),$$

   where the indices $i \pm \frac{1}{2}$ are computed using an upwind-method. For instance,

$$i + \frac{1}{2} = \begin{cases} i+1 & \text{if } \cos(\theta_s) \leq 0 \\ i & \text{if } \cos(\theta_s) > 0 \end{cases}$$

Remark A.1 *To estimate the coefficients* $\{c_k\}_k$ *in* (A.1), *we need to perform a change of coordinates which creates error if* $\overline{\theta}$ *is not a meshgrid point. To avoid those interpolations approximations, we use a change of coordinates in the formula* (A.1)

$$c_k = \sum_s f(\theta_s) P_{-k}(\theta_s - \overline{\theta}) \frac{\Delta\theta}{M(\theta_s - \overline{\theta})}. \tag{A.2}$$

Since P_n *and* M *are explicit functions* (3.4) (3.13), *there is no additional cost in using* (A.2).

B Stability for the homogeneous equation

To implement the numerical scheme (3.24) for the homogeneous equation $\partial_t f = Q(f)$, we have to establish a stability condition. The explicit Euler method is stable under the condition that:

$$|\lambda_{Max}|\,\Delta t < 1,$$

where λ_{Max} is the largest eigenvalue of the matrix $[Q]_{\mathcal{B}}$ (3.19). From the Gershgorin circle theorem, we find a rough estimate as: $|\lambda_{Max}| \sim \frac{\sigma}{4}N^2$. This rough estimation is confirmed numerically (see figure 11).

Analytically, the solution f is converging toward an equilibrium (3.3). Thus, one needs to verify that Q has a zero eigenvalue. Numerically (see figure 11), the first eigenvalue λ_1 decreases with the number of discretization intervals N and stabilizes for $N > 20$ near machine precision around 10^{-15}.

Therefore, we use in our simulation $N = 32$ discretization intervals for the angle velocity θ. For the time discretization, we ensure that $\frac{\sigma}{4}N^2\Delta t < 1$ once we use the explicit Euler scheme. There is no such constraint if we use the implicit Euler method.

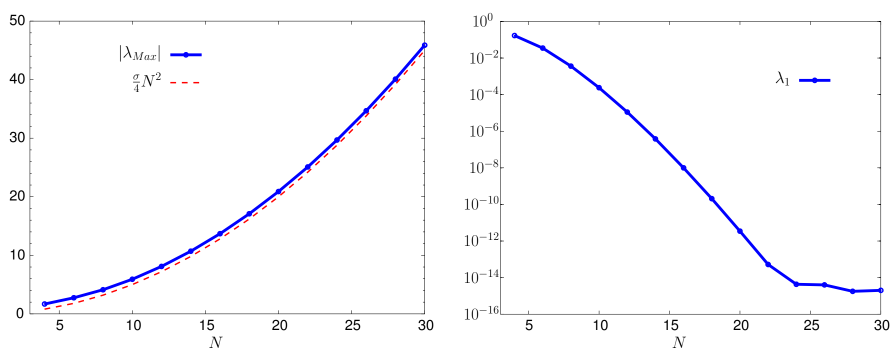

Figure 11: **Left:** the largest eigenvalue λ_{Max} of $[Q]_{\mathcal{B}}$ (3.19) depending on N the number of points of discretization of the angle velocity $\theta \in (-\pi, \pi]$. **Right:** the first eigenvalue λ_1 of $[Q]_{\mathcal{B}}$ depending on N.

C Accuracy of the numerical scheme (homogeneous case)

To measure the accuracy of the scheme, we take advantage that the solution of the homogeneous equation has to converge to equilibrium (a Von Mises distribution M (3.3)). In figure 12, we measure the distance between the solution $f(t, \theta)$ of the homogeneous equation and the corresponding equilibrium (i.e. $\|f(t,.) - M\|_H$) at different times ($T = 10$, 20, 50) and for different number of modes N. We observe that at large time $T = 50$ (red curve), the distance is decaying exponentially fast with the number of modes. The distances reaches eventually 10^{-14} due to machine precision error. This result is consistent with the accuracy of spectral methods [1, 19, 33]. At time $T = 10$ and 20, the solution $f(t, .)$ has not yet reached a stationary state. Thus, even though we increase the number of modes N, the distance does not decrease to zero.

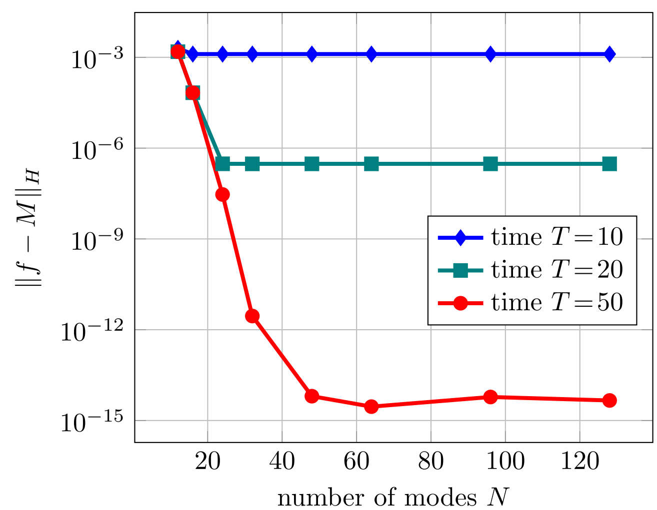

Figure 12: Distance between the homogeneous solution $f(t, \theta)$ and the Von Mises distribution M (3.3). At time $T = 50$ (red curve), the distance is decaying exponentially fast with the number of modes (N). Parameters for the simulation: $\sigma = .2$, $\Delta t = .1$.